The assessment of the severity of local impact on a pro-bionic composite lattice shell by the use of fiber-optic sensors

S.B. Sapozhnikov
South Ural State University (National research university), Chelyabinsk, Russia
Central aerohydrodynamic institute (TsAGI), Zhukovsky, Russia
sapozhnikovsb@susu.ru, https://orcid.org/0000-0002-7022-4865

E.A. Dubovikov
Central aerohydrodynamic institute (TsAGI), Zhukovsky, Russia
evgeny.dubovikov@tsagi.ru, https://orcid.org/0000-0001-9402-3649

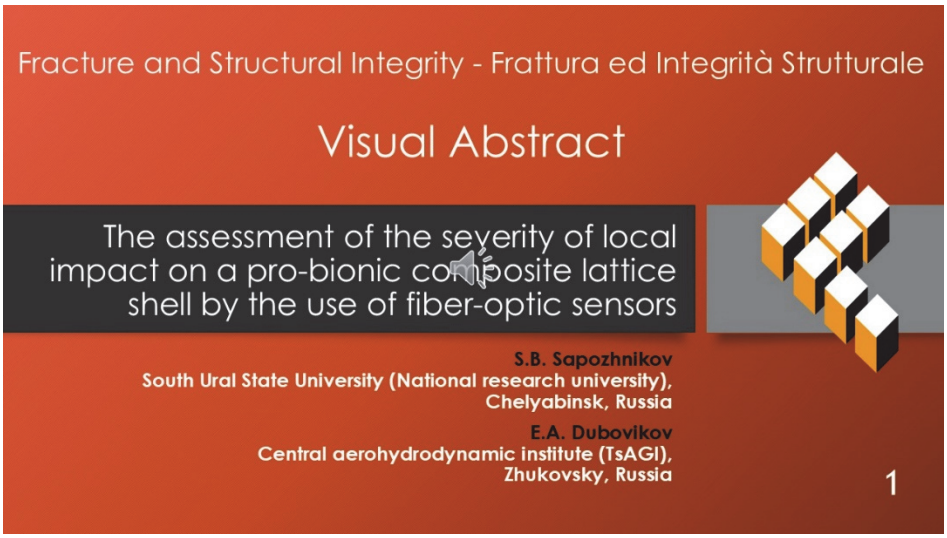

Citation: Sapozhnikov, S.B., Dubovikov E.A., The assessment of the severity of local impact on a pro-bionic composite lattice shell by the use of fiber-optic sensors, Fracture and Structural Integrity, 73 (2025) 1-11.

Received: 28.02.2025
Accepted: 27.03.2025
Published: 05.04.2025
Issue: 07.2025

KEYWORDS. Lattice shell, Local impact, Fiber optic sensor, Thermoplastic protective tab, Residual strain.

INTRODUCTION

The health of critical composite structures is impossible without installing sensors based, for example, on fiber optic, strain gauges or piezoelectric sensors in critical areas [1-3]. A request to SCOPUS on the topic of fiber optic sensor (FOS) for aerospace revealed more than 1000 publications, demonstrating a steady growth, starting from one in 1984 to 177 publications in 2024.

Information from the installed FOS is recorded and processed in order to determine the place of a local impact [4,5], the size of a defect like delamination [4-7] or the approach to catastrophic failure [8,16]. The FOS item in the mechanics of composites is not complete, developing to wider strain or thermal range [20-22], to measure of magnetic fields [20,23], to solve problems of visualization of measuring results and machine learning [19,24], to fastening measurement process and miniaturization of FBG sensors [25], to getting higher accuracy by doping of nanoparticles [26].

For aircraft structures, local impacts by foreign bodies are dangerous due to the fragility of composites based on carbon-, glass- or organic fibers [9]. It forces the introduction of additional safety factor and reduces the potentially high weight efficiency of composite structures. To solve the above-mentioned problems, relatively recently pro-bionic lattice shells (PBLS) have been proposed [10-12], containing not two, but three systems of load-bearing ribs made of UD composite, protective tabs on the ribs and an outer elastic skin to take aerodynamic forces. The load-bearing ribs are located deeper in the structure and protected from external impacts by the skin lying on the protective tab, Fig. 1. In this case, the use of traditional non-destructive testing technics like ultrasound or thermal vision is impossible.

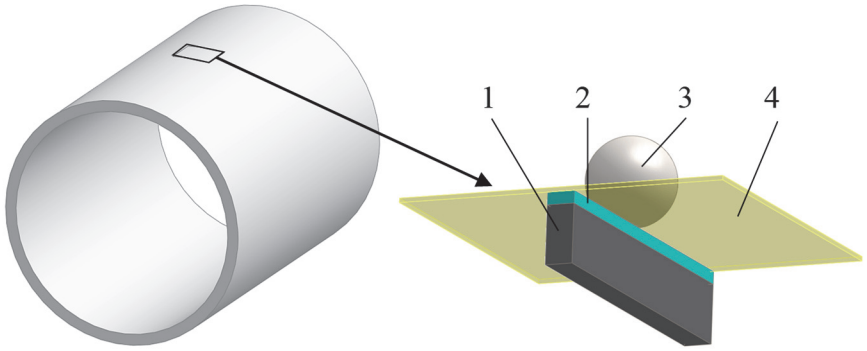

Figure 1: The PBLS and its fragment: rib (1), protective tab (2), impactor (3) and skin (4).

During a local impact, the elastic skin bends without breaking, and the tab dampens the impact, extending the contact time and reducing the contact load [11,12].

In the practice of testing of aircraft composite elements, the concept of a "standard impact" is used, i.e. a low-velocity impact by a falling body with a given energy, which should not damage the load-bearing elements [13-15]. In this work, these are the ribs of the PBLS, protected by special tabs made of thermoplastic material. According to the aim of this article, it needs to use these tabs also as sensing media of impact, carrying embedded FOS.

At the same time, questions remain open: what parameters should the damping tab have, what happens to the PBLS elements after the impact, where did the impact occur, can FOS (Bragg or Brillouin) register residual strain of the load-bearing rib?

This paper attempts to answer these questions based on numerical modeling of the low-velocity impact process.

MODELING

There are two tasks here: the first is to justify the cutting of a small enough volume from a whole shell for detailed study of the stress state and the second - correctly assign boundary conditions for that detailed volume.

Smooth shell

For an estimate of the contact time, the magnitude of the loads acting in the "impactor - shell" contact, we will represent the PBLS with an isogrid mesh of ribs as a smooth shell made of a quasi-isotropic equivalent material [10,17]. Elastic modulus and Poisson's ratio of that material are calculated using the dependencies

$$E = A_{11} - \frac{A_{12}^2}{A_{22}}, \quad \mu = \frac{A_{12}}{A_{22}} \tag{1}$$

Here

$$A_{11}=\sum_{i=1}^{n}\frac{1}{a_i}E_i\delta_i\cos^4\varphi_i,\quad A_{12}=\sum_{i=1}^{n}\frac{1}{a_i}E_i\delta_i\sin^2\varphi_i\cos^2\varphi_i \tag{2}$$

The density of the equivalent shell material is

$$\rho=\sum_{i=1}^{n}\frac{\delta_i}{a_i}\rho_i \tag{3}$$

Parameters of the lattice shell: a, δ, φ, E and ρ – distance between ribs, width, lay-up angle with the longitudinal axis of the shell, modulus of elasticity and density of the material of the rib of the i-th family. All ribs have the same height h.

If the parameters of the lattice shell are known and, for example: φ=90°,+30°,–30° (isotropic scheme), the smooth shell should be made of a virtual material with E=5.2 GPa, μ=0.333, ρ=0.15 g/cm3.

Next, let's look at the shell (wide body civil aircraft fuselage) with an outer diameter D=4 m and a length L=12 m, subjected to a local impact by a steel sphere with a diameter of 50.8 mm (weight 0.539 kg) with different energies E=5, 10, 20 and 50 J.

Fig. 2 shows the scheme of the problem, in which the geometry was created in the SolidWorks software (thin shell and solid sphere). Numerical calculations were performed in the ANSYS (explicit dynamics). The total process time t=2 ms, the impactor velocities before contact V=4.33; 6.12; 8.66 and 13.7 m/s.

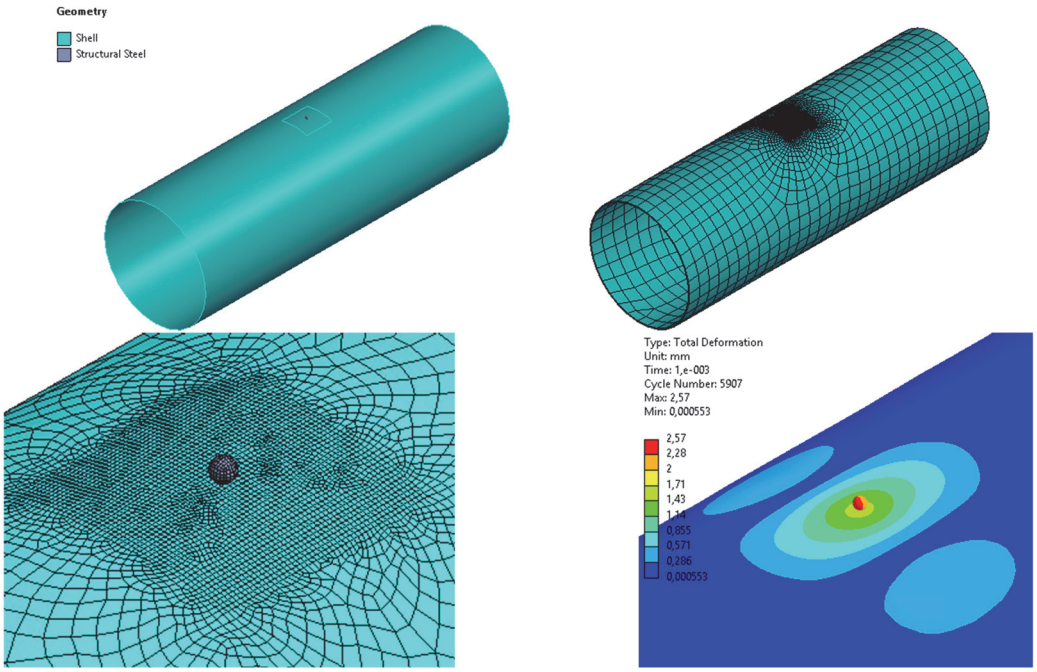

Figure 2: Model, FE mesh, detailed zone and deflection picture (V=4.33 m/s) of the shell at t=1 ms.

Fig. 3 shows the dependences of the impactor velocity V(t), the displacement of the shell during contact and the contact force P(t) obtained by calculation based on the FEM data using numerical differentiation of V(t)

$$P(t)=m\cdot a(t),\ a(t)=\frac{dV(t)}{dt} \tag{4}$$

The maximum contact force is about 3.2 kN, and the maximum deflection of the shell at the point of contact is 1.59 mm. The coefficient of restitution - the ratio of the rebound velocity (0.98 m/s) to the initial velocity (4.33 m/s) is 0.226. In other words, almost 80% of the energy of the falling body is converted into the energy of shell deformation.

For other impact energies, the results are qualitatively the same. Tab. 1 shows the generalized calculation results. The contact time in all cases is about 1.51 ms.

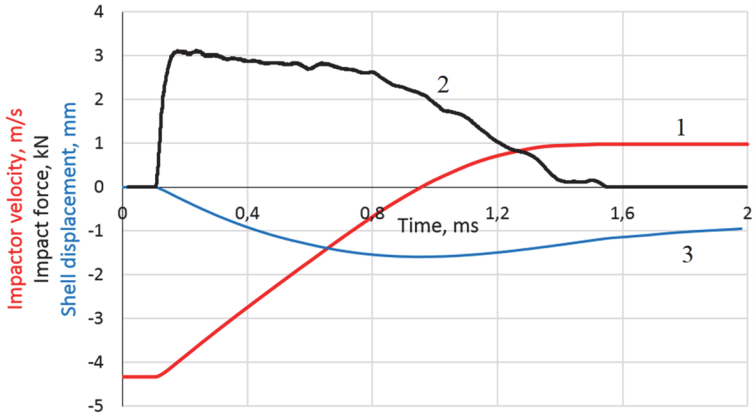

Figure 3: Model, FE mesh, detailed zone and deflection picture (V=4.33 m/s) of the shell at t=1 ms.

Impact energy, J	Impactor velocity, m/s	Contact force, kN	Shell displacement, mm	Recovery coefficient, -	Contact time, ms
5	4.33	3.20	1.59	0.226	1.50
10	6.12	4.2	2.24	0.269	1.51
20	8.66	6.40	3.27	0.275	1.51
50	13.7	10.01	5.27	0.269	1.54

Table 1: Calculation results.

Detailed modeling of the PBLS fragment

Next, we will consider quasi-static loading of a fragment of the mesh shell with the found forces. The fragment has hinged support at the edges, based on the nature of the shell bending during the impact, Fig. 4 (cross section, amplification of displacements by 50 times).

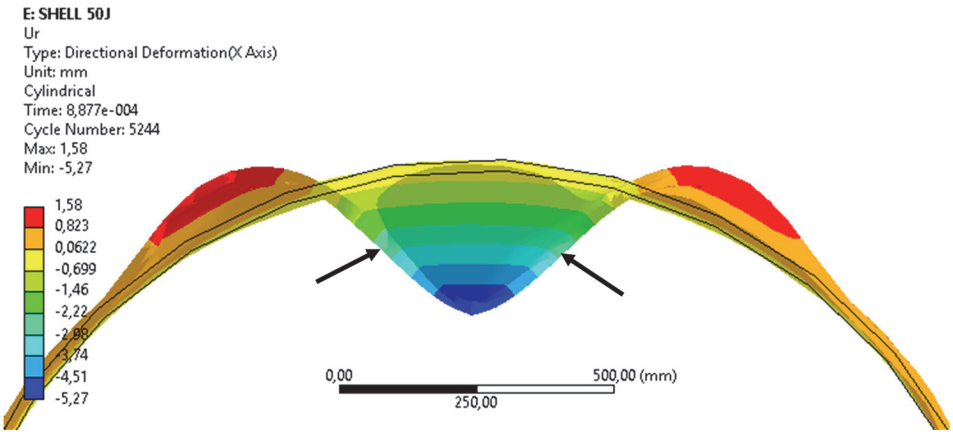

Figure 4: Deformation of the shell under local impact. Time 0.8877 ms.

Here we can see the change in the sign of the curvature - from positive to negative (see arrows), which allows us to find the correct boundary conditions - the position of the hinge supports for simplified modeling of the fragment's deformation. The fragment has two planes of symmetry, so it is rational to consider ¼ of the part, Fig. 4. It is important to note that the PBSO rib is made layered, consisting of a unidirectional composite and a polymer matrix, which reflects the technology of wet winding of a lattice shell with carbon fiber bundles.

In [18], it was shown that the presence of layers of a polymer matrix during transverse compression of the rib creates additional tension of the composite layer across the fibers (in the plane of the layer), halving the rib's fracture stress.
The protective tab is made of thermoplastic PA6 with a thickness of 5 mm, and the skin is made of 3D-woven aramid FRP with a thickness of 1.5 mm. The steel indenter has a diameter of 2 inches (50.8 mm). A force of 10.01/4=2.5 kN is applied to the indenter corresponding to the case with an impact energy of 50 J.

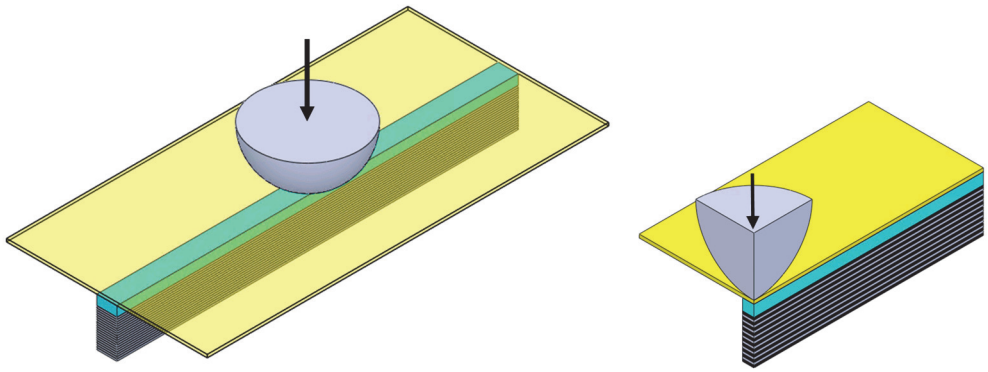

Figure 5: Fragment of the PBSO (total length 200 mm, left) and its ¼ part for calculations (right).

The loading program consisted of two stages: increasing the force to a value of 2.5 kN and unloading. The materials of the tab and polymer matrix were assumed isotropic elastic-plastic with a bilinear diagram. Tab. 2 shows the elasticity parameters of the models of all materials, and Tab. 3 - the strength parameters. Here σY - yield strength, ES is the tangent modulus at the stage of plastic deformation, e* is the failure strain. Carbon fiber reinforced plastic (CFRP) and aramid fabric reinforced plastic (AFRP) are orthotropic materials (9 elasticity characteristics and 9 strength characteristics along main axis of materials).

Material	density	E_1	E_2	E_3	G_{12}	G_{23}	G_{13}	μ_{12}	μ_{23}	μ_{13}
	g/sm³		GPa			GPa			-	
UD CFRP	1.55	200	8.6	8.6	4.7	4.7	4.7	0.27	0.40	0.27
AFRP*	1.30	10	10	5	2	2	2	0,04	0.3	0.3
Resin epoxy	1.16		3.78			-			0.35	
PA6	1.20		2.0			-			0.40	
Steel	7.85		200			-			0.30	

*3D-weaving, low elastic modulus (polyurethane matrix)

Table 2: Elasticity characteristics (for evaluation only).

Material	F_{1t}	F_{1c}	F_{2t}	F_{2c}	F_{3t}	F_{3c}	F_{12}	F_{23}	F_{13}
					MPa				
UD GFRP	2000	1000	60	200	60	200	70	60	70
AFRP*	1500	800	1500	800	200	300	50	50	50
Resin epoxy		σ_Y=60 MPa			Es= 1000 MPa			e*=0.05	
PA6		σ_Y=40 MPa			Es=300 MPa			e*=0.20	
Steel		-			-			-	

Table 3: Strength characteristics (for evaluation only).

Fig. 6 shows the boundary conditions and the finite element (FE) mesh. It is important to note that the share topology option (ANSYS, SpaceClaim module) was used when creating the model to have common nodes on the layer interfaces and to exclude operations with contact algorithms. It significantly decreases the calculation time for geometrically and physically nonlinear problems. Frictionless contact is established between the indenter and the skin.

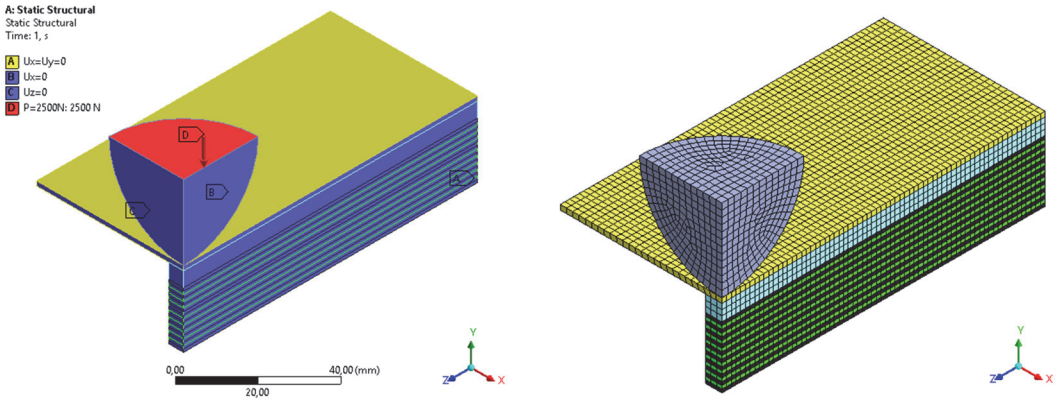

Figure 6: Boundary conditions and FE mesh.

The calculations were performed in the ANSYS on a multiprocessor cluster of South Ural State University. The results of calculating the displacements and stresses in the fragment elements are shown in Figs. 7-9.

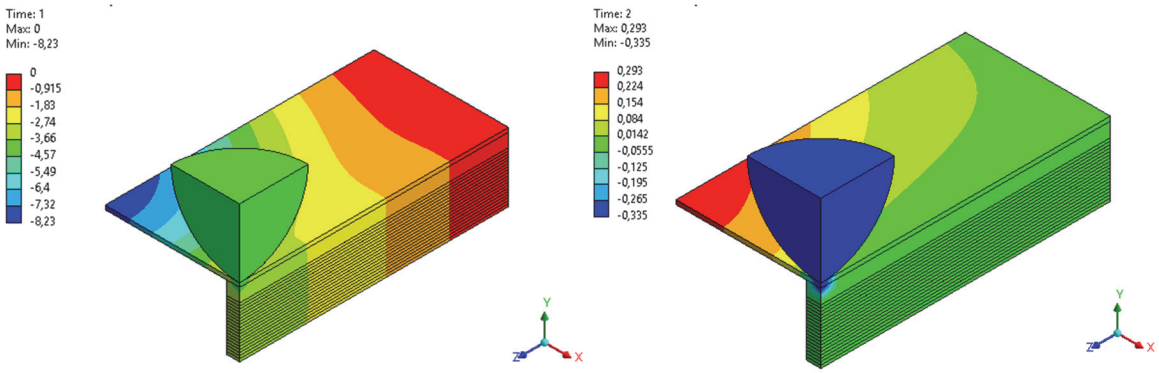

Figure 7: Displacement pictures at t=1 s (maximum load) and t=2 s (complete unloading).

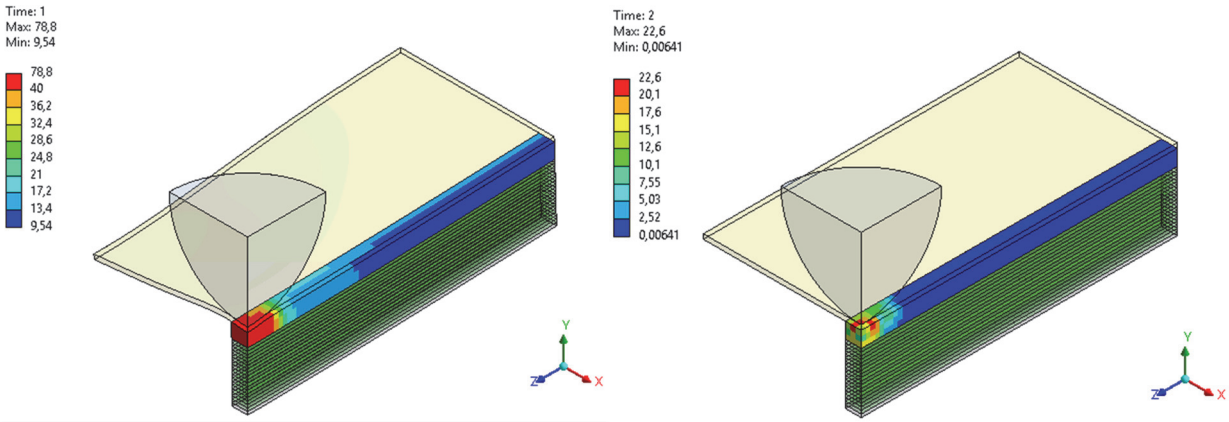

Figure 8: Pictures of von Mises stresses in the tab at t=1 s (maximum load) and t=2 s (complete unloading).

In Fig. 8, the yield zone (stresses above 40 MPa) is marked in red on the left. On the right is the picture of residual stresses in the tab.

Obviously, the presence of residual stresses allows asserting the possibility of recording residual deformations and localizing the impact site using the FOS. Fig. 9 shows the distribution of maximum and residual deformations in carbon fiber layers. It can be seen that after unloading, the level of strain on the lower surface of the rib is 0.03-0.04%, which is close to the detection limit of the FOS.

It follows that the sensors should be located into the body of the tab at the contact surface with the skin. Fig. 10 shows the distribution of strain in the skin.

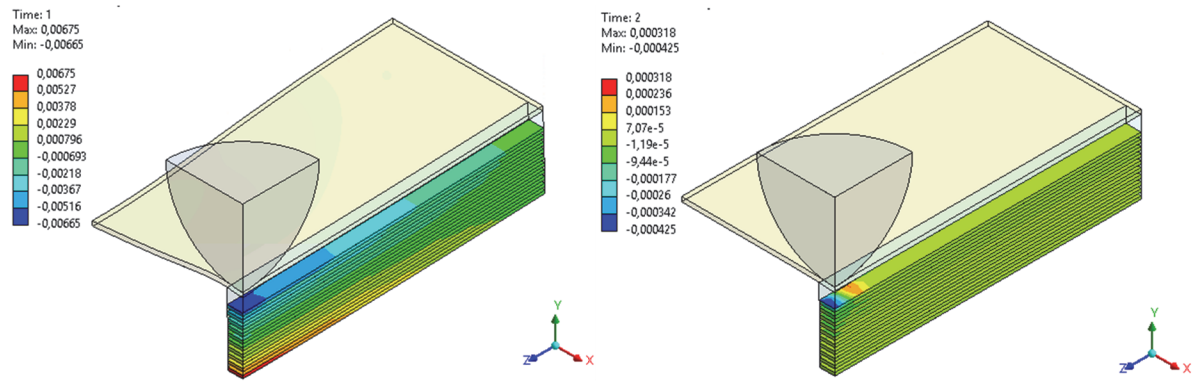

Figure 9: Longitudinal deformations in composite layers at t=1 s (maximum load) and t=2 s (complete unloading).

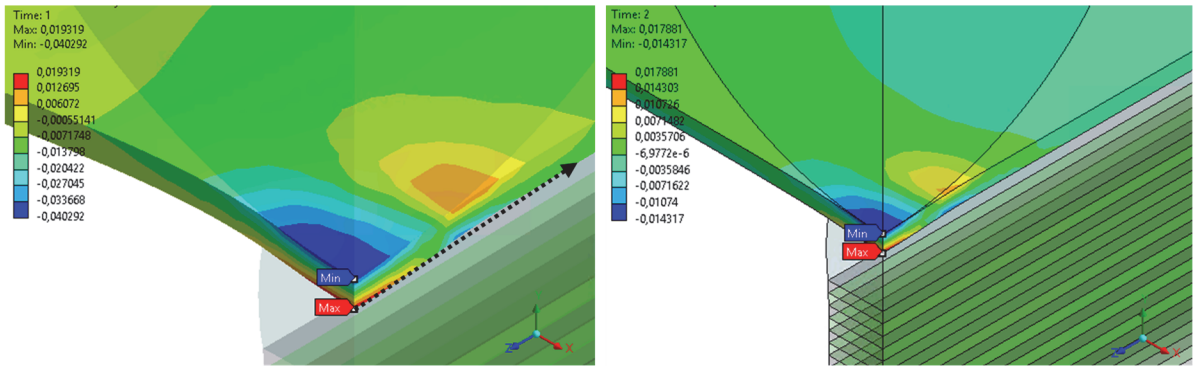

Figure 10: Distribution of strain in the skin at t=1 s (maximum load) and t=2 s (complete unloading).

Discussion

The distribution of strain along the contact line of the skin with the tab (dotted arrow, Fig. 11) is shown in Fig. 11. Near the contact point, the strain reaches 2%, which is acceptable for the FOS. After unloading, the maximum residual strain is about 0.5%. This value can be reliably recorded by the FOS. The measurement step should be no more than 15 mm in order to record the impact point with an error of ±7.5 mm.

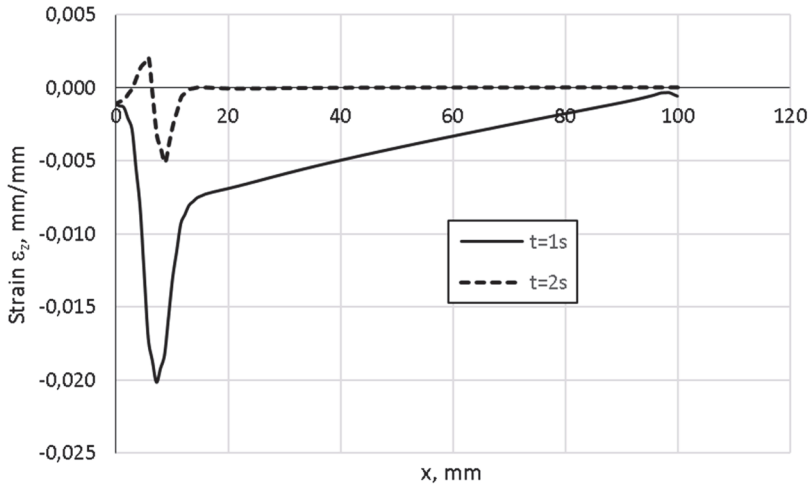

Figure 11: Strain along the contact line of the tab with the skin (50 J).

With an impact with less energy (20 J), the FOS will show smaller strain along the contact line of the tab with the skin, Fig. 12.

Tab. 4 shows the dependences of the maximum values of longitudinal strain in the tab material upon impact and the maximum residual values as a function of the impact energy.

The stress state in the UD CFRP rib layers is shown in Fig. 13. The danger is posed by the compression stresses along the fibers of the upper layer, which are close to the strength limit, as well as the stresses across the fibers, which exceed the tensile strength of the UD CFRP (Tab. 3).

Analysis of these results shows that when impact has an energy of 50 J, the upper layer of CFRP cracks along the fibers and may lose stability when compressed.

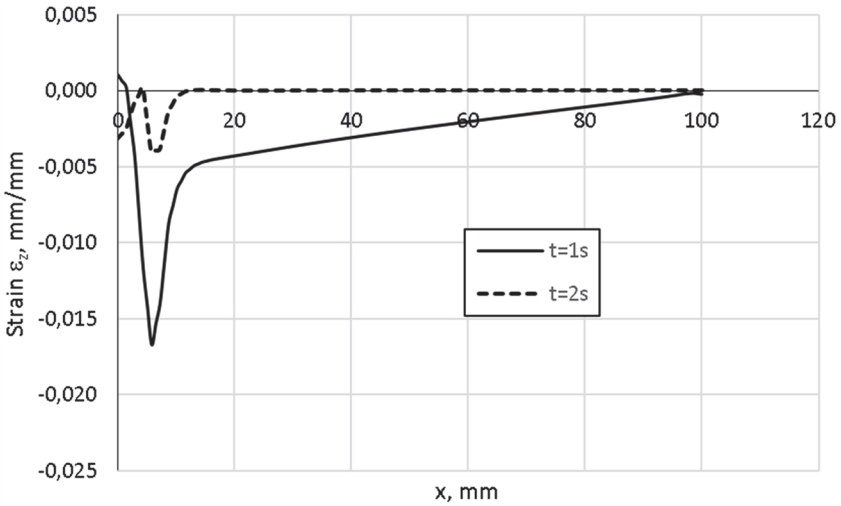

Figure 12: Strain along the contact line of the tab with the skin (20 J).

Impact energy, J	5	10	20	50
Maximum strain, %	1.35	1.67	2.05	2.57
Residual strain, %	0.57	0.83	1.28	2.07

Table 4: Strain in the impact zone.

It follows that the protective tab material should not have large transverse strain to avoid cracking of the UD CFRP along the fibers.

For this purpose, it is proposed to install a thin layer (0.5 mm) of fabric AFRP under the tab, Fig. 14, and reduce the thickness of the pad from 5 to 4 mm.

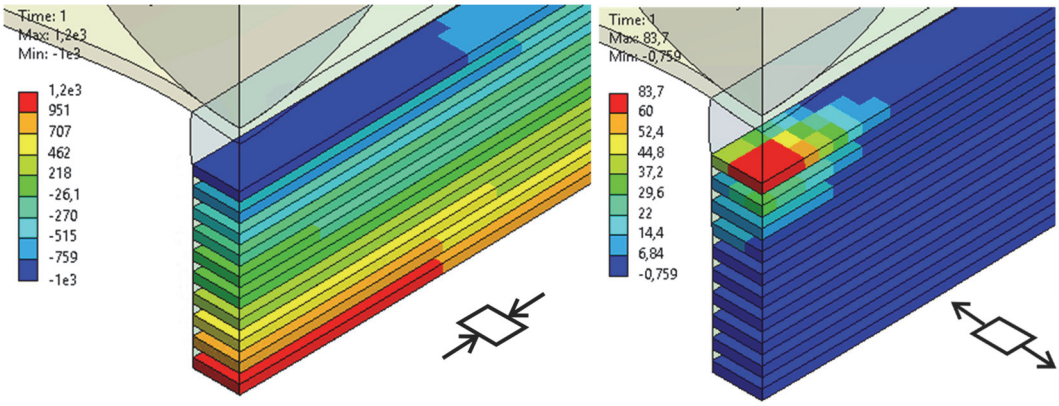

Figure 13: Stress state in UD CFRP layers (50 J).

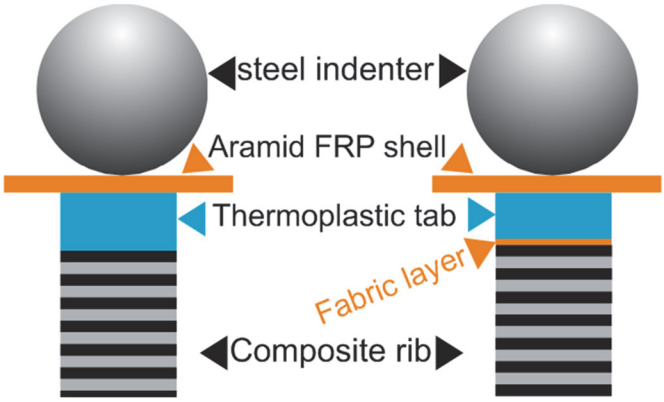

Figure 14: Typical (left) and new (right) design.

The elastic moduli of fabric AFRP for the warp and weft are E1 = E2 ≈ 30 GPa and this will restrain the transverse strain of the thermoplastic tab, Fig. 15.

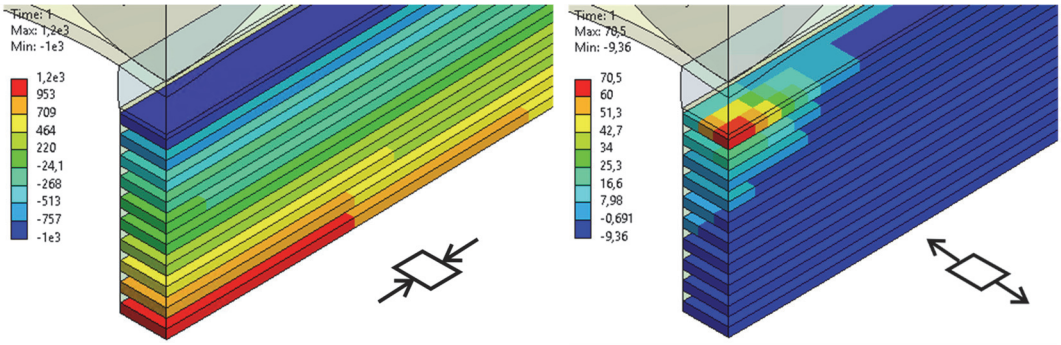

Figure 15: Stress state in UD CFRP layers (50 J).

It can be seen that the stresses along the fibers have not changed, and across the fibers have decreased to a safe level. With this modification, the skin strain at the boundary with the thermoplastic tab have remained virtually unchanged, Fig. 16 (see also Fig. 11).
A slight increase in maximum strain is observed (from 2 to 2.1%), which is not critical for the strength of the optical fiber.

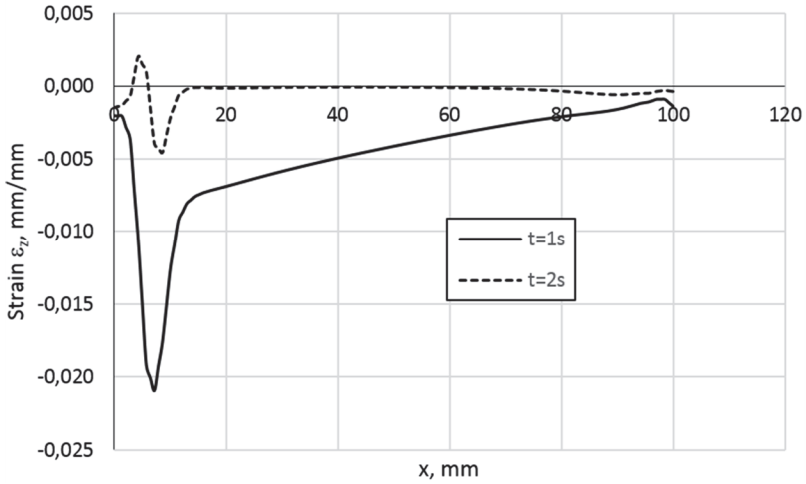

Figure 16: Deformations along the contact line of the pad with the skin (50 J).

CONCLUSIONS

In the paper, the finite element analysis of the overall loading of a cylindrical ribbed shell with a diameter of 2 meters under a low-velocity local impact with an energy of up to 50 J was performed.

To get detailed information about state of the ribs under impact, it was offered a two-stage scheme, where the first stage was devoted to investigation of smooth shell (with a stiffness equivalent to ribbed one) under impact and determine the maximum load in dynamic contact. The second stage was devoted to detailed quasi-static loading with maximum load and unloading to assess the residual strain state of a fragment containing a layered UD CFRP rib measuring 10x20 mm, a protective tab made of PA6 thermoplastic with a thickness of 5 mm and an external skin made of AFRP with a thickness of 1.5 mm.

It was found that the placement of the fiber optical sensor (FOS) for recording residual strain in the impact zone should be in the upper part of the tab at the contact with the skin.

In the case of a local impact with an energy of 50 J, the maximum strain of the FOS will not exceed 2%, and the residual strain of FOS will be about 0.5%. When placing the FOS in the middle of the tab, the maximum strain will increase to 2.6% (close to failure), and the residual one will be about 2%.

There is a monotonic function of the residual strain of the tab on the impact energy. When the impact energy decreases from 50 to 5 J, the residual strain in the tab decrease from 2.07 to 0.57%.

It is also shown that, under an impact with an energy of 50 J, the failure of the first layer of UD CFRP in the rib can be avoided if the protective tab made of PA6 with a thickness of only 4 mm contains a fabric tape made of AFRP with a thickness of 0.5 mm at the bottom, restraining its transverse strain in the local impact zone.

Moreover, to register a residual strain near the local impact place, which is not known before, it is better to use a distributed FOS (Brillouin) rather than Bragg's one (FBG) needed to know exact place for strain measurement .

ACKNOWLEDGMENTS

The work was carried out as part of a major scientific project of Ministry of science and higher education of the Russian Federation (Agreement No. 075-15-2024-535 dated 23 April 2024).

REFERENCES

[1] Rocha, H., Semprimoschnig, C., Nunes, J.P. (2021) Sensors for process and structural health monitoring of aerospace composites: A review, Engineering Structures, 237, 112231.

[2] Vorathin, E., Hafizi, Z.M., Che, S.A., Ghani, K.S. (2016) Lim real-time monitoring system of composite aircraft wings utilizing Fibre Bragg Grating sensor, IOP Conference Series: Materials Science and Engineering, 152 (1), 012024.

[3] Takeda, N. (2008) Fiber optic sensor-based SHM technologies for aerospace applications in Japan, Proceedings of SPIE - The International Society for Optical Engineering, 6933, 693302.

[4] Goossens, S., Berghmans, F., Muñoz, K., Jiménez, M., Karachalios, E., Saenz-Castillo, D., Geernaert, T. (2021) A global assessment of barely visible impact damage for CFRP sub-components with FBG-based sensors, Composite Structures, 272, 114025.

[5] Datta, A., Augustin, M.J., Gupta, N., Viswamurthy, S.R., Gaddikeri, K.M., Sundaram. R. (2019) Impact localization and severity estimation on composite structure using Fiber Bragg Grating sensors by least square support vector regression, IEEE Sensors Journal, 19 (12), pp. 4463-4470.

[6] Díaz-Maroto, P.F., Fernández, A., Larrañaga, B., Guemes, A. (2016) Free-edge delamination location and growth monitoring with an embedded distributed fiber optic network, 8th European Workshop on Structural Health Monitoring, EWSHM 2016, 2, pp. 993-1001.

[7] Sun, C.T., Dicken, A., Wu, H.F. (1993) Characterization of impact damage in ARALL laminates, Composites Science and Technology, 49 (2), pp. 139-144.

[8] Nyman, T., Bredberg, A., Schön, J. (2000) Equivalent damage and residual strength for impact damaged composite structures," Journal of Reinforced Plastics and Composites, 19 (6), pp. 428-448.

[9] Chen, V.L., Wu, H.-Y.T., Yeh, H.-Y. (1993) A parametric study of residual strength and stiffness for impact damaged composites, Composite Structures, 25 (1-4), pp. 267-275.

[10] Vasiliev, V.V., Barynin, V.A., Razin, A.F. (2012) Anisogrid composite lattice structures - development and aerospace applications, Composite Structures, 94 (3), pp. 1117-1127.
[11] Shanygin, A., Zichenkov, M., Kondakov, I. (2014) Main benefits of pro-composite layouts for wing and fuselage primary structure units, 29th Congress of the International Council of the Aeronautical Sciences, ICAS 2014.
[12] Kondakov, I.O., Chernov, A.V., Shanygin, A.N., Sapozhnikov, S.B. (2022) Protection of aircraft lattice shell made of UD CFRP ribs from Low-Velocity Impacts, Mechanics of Composite Materials, 57 (6), pp. 721-730.
[13] Chaumette, D. (1985) Certification problems for composite airplane structures, Materials Science Monographs, 29, pp. 19-28.
[14] Ilcewicz, L.B., Murphy, B. (2005) Safety & certification initiatives for composite airframe structure, Collection of Technical Papers - AIAA/ASME/ASCE/AHS/ASC Structures, Structural Dynamics and Materials Conference, 2, pp. 887-898.
[15] Zhuguo, Z., Yingchun, Z., Xupo, O. (2011) Study on key certification issues of composite airframe structures for commercial transport airplane, Procedia Engineering, 17, pp. 247-257.
[16] Serioznov, A.N., (2016) Application of fiber optic technologies in the creation of built-in self-diagnostic systems for aircraft structures, Novosibirsk, Scientific Bulletin of NSTU, 64(3), pp. 95-105, in Russian.
[17] Vasiliev, V.V. (1988) Mechanics of structures made of composite materials, Moscow, Mashinostroenie, 270 pp., in Russian.
[18] Sapozhnikov, S.B., Shaburova, N.A., Ignatova, A.V., Shanygin, A.N. (2022)Analysis of the mesostructure and fracture kinetics of elements of lattice composite structures under transverse compression using stochastic FEM micromechanics, Bulletin of Perm National Research Polytechnic University. Mechanics, 4, pp. 54–66.
[19] Marceddu, A.C., Aimasso, A., Bertone, M., Viscanti, L., Montrucchio, B., Maggiore, P., Dalla Vedova, M.D.L. (2024) Augmented reality visualization of fiber Bragg grating sensor data for aerospace application, IEEE International Workshop on Metrology for AeroSpace, MetroAeroSpace 2024. Proceeding, pp. 519-524.
[20] Berthold III, J.W. (2024) Fiber optic sensors: an introduction for engineers and scientists, Third Edition, pp. 573 – 591.
[21] Hu, C., Du, A., Yang, L., Yang, B. (2024) Research progress on health monitoring techniques for composite pressure structures, Chinese Quarterly of Mechanics, 45 (3), pp. 593-613.
[22] Aimasso, A., Dalla Vedova, M.D.L., Bertone, M., Maggiore, P. (2024) Preliminary design and performance evaluation of optical fiber-based load sensor for aerospace systems, Journal of Physics: Conference Series, 2802 (1), 012010.
[23] Li ,Y., Jia, X., Li, L., Hu, D. (2024) Application of FBG sensing technology in flight test strain measurement, IEEE 6th International Conference on Power, Intelligent Computing and Systems, ICPICS, pp. 1485-1489.
[24] Gupta S., Kumar B., Mishra S. (2024) Machine learning enabled FBG optical sensor applications, 2nd International Conference on Advancements and Key Challenges in Green Energy and Computing, AKGEC 2024.
[25] Li, C., Tong, X., Huang, W., Wang ,Y., Zeng, F., Chen, L., Shi, X., Zeng, C. (2024) Development of a fast response, high accuracy, and miniaturized fiber Bragg grating (FBG) sensor for fluid temperature measurement, IEEE Sensors Journal, 24 (6), pp. 8746-8753.
[26] Wang, X., Xiao, Y., Rans, C., Benedictus, R., Groves, R.M. (2024) Enhanced strain measurement sensitivity with gold nanoparticle-doped distributed optical fibre sensing, Structural Control and Health Monitoring, 2716156.